Journal of Fluids and Structures 139 (2025) 104432

Contents lists available at ScienceDirect

Journal of Fluids and Structures

journal homepage: www.elsevier.com/locate/yjfls

Stably biased gap flow between two flapping and stationary short cantilevers in close proximity

Yongpu Wang [a,b], Yanyan Liu [a,b], Michael David Atkins [c], Tian Jian Lu [a,b], Tongbeum Kim [a,b,*]

[a] MIIT Key Laboratory of Multifunctional Lightweight Materials and Structures, Nanjing University of Aeronautics and Astronautics, Nanjing 210016, China
[b] College of Aerospace Engineering, Nanjing University of Aeronautics and Astronautics, Nanjing 210016, China
[c] School of Mechanical, Industrial and Aeronautical Engineering, University of the Witwatersrand, Johannesburg 2000, South Africa

ARTICLE INFO

Keywords:
Vortex shedding
Biased gap flow
Flow-induced flapping
Kelvin-Helmholtz instability
Fluid-structure interaction

ABSTRACT

Contrary to previously known physics about fluid motion around two side-by-side circular cylinders, this study has demonstrated stably biased gap flow when excited by a flapping and stationary cantilever pair - the gap flow is only deflected towards the flapping cantilever (without switching). Mechanisms for this behavior were presented in this study. To this end, flow visualization and spectral analysis of time-resolved data from hot-wire anemometers and the piezoelectric mount of a flapping cantilever were carried out. Furthermore, particle image velocimetry was conducted to map instantaneous and time-averaged velocity and vorticity fields. During measurements, a center-to-center spacing normalized by cantilever diameter (T/D, pitch ratio) was systematically varied in the Reynolds number range of $1800 \leq Re_D \leq 13{,}000$. We demonstrated that the Kelvin-Helmholtz (K-H) instability of shear layers separated from the flappable cantilever was intensified due to flapping, consequently inciting the earlier onset of Kármán vortices (evolved from K-H vortices) than those behind the stationary cantilever. Thereafter, an earlier velocity recovery developed, generating a transverse pressure gradient towards the flapping cantilever and subsequent upstream penetration (i.e., potential effect). The gap flow then became stably pushed towards the flapping cantilever.

1. Introduction

Flow around two side-by-side circular cylinders is a configuration that has been extensively studied to understand the physics of fluid motion around multiple bluff bodies in close proximity to one another. Multiple bluff bodies have many practical applications, e.g., the design of nuclear reactor cores, off-shore drilling platforms, heat exchanger tube bundles, and power transmission lines (Zdravkovich, 1997; Sumner et al., 1999; Wang et al., 2020). Side-by-side cylinders are also relevant in a renewable energy harvesting scheme, e.g., the motion of one cylinder or both cylinders induced by a wind current to extract the associated kinetic energy (Lee et al., 2019).

The spacing between the two cylinders is known to strongly affect the wake shedding behavior, particularly when the gap falls

* Corresponding author.
E-mail addresses: ypwang@nuaa.edu.cn (Y. Wang), liuyanyan@nuaa.edu.cn (Y. Liu), Michael.Atkins@wits.ac.za (M.D. Atkins), tjlu@nuaa.edu.cn (T.J. Lu), tongbeum.kim@nuaa.edu.cn (T. Kim).

https://doi.org/10.1016/j.jfluidstructs.2025.104432
Received 23 February 2025; Received in revised form 29 May 2025; Accepted 24 September 2025
Available online 29 September 2025
0889-9746/

within the range of 1.1~1.2 ≤ T/D (defined herein as the pitch ratio) ≤ 2.0~2.5, where asymmetric wakes develop with respect to the axis of symmetry seen in Fig. 1(a) (Sumner et al., 1999; Zdravkovich 1988; Brun et al., 2004; Atkins et al., 2016). Here, T is the center-to-center distance (i.e., pitch) while D is the diameter of a single cylinder. The wake patterns are characterized by a narrow near-wake region behind one cylinder and a wide wake region behind the other one, where the shedding rate of narrow wakes is higher than wide wakes. The narrow wake shedding frequency (f_n) is greater than the reference shedding rate, observed behind a single cylinder in isolation with the same diameter of D. In contrast, the wide wake shedding (f_w) is less than the single isolated cylinder (f_s). Importantly, the narrow and wide wake patterns switch from one cylinder to the other at irregular time intervals, often referred to as "flip-flopping" (Kim and Durbin, 1988; Miau et al., 1992). These two wakes are coupled by flow bled through a gap (= T - D) between the two side-by-side cylinders, which is called the "gap flow." Therefore, this gap flow is seen as being biased towards one cylinder and displays random switching. It was recent that a third wake pattern was observed, whereby the gap flow was intermittently aligned to be parallel with the freestream flow, and intermediate width wakes and shedding rate equal to the reference single cylinder (i.e., intermediate wake pattern) appeared (Alam et al., 2003; Wang et al., 2025). Thus, the wake patterns are, strictly, tri-stable. It should be pointed out that, in most literatures, it is often referred to as bi-stable, ignoring the intermediate wake pattern.

A notable study by Kim and Durbin (Kim and Durbin, 1988) argued that the asymmetric wake patterns and their switching event are attributed to a Poisson stochastic process. They conjectured that switching, or flip-flopping, was the behavior of a simple dynamical system between two quasi-stable states. However, no further physical explanation was given to describe the mechanisms of the switching process. Other efforts made include a study by Ishigai et al. (Ishigai et al., 1972) who deemed the mechanism for the formation of biased (strictly speaking, bi-stable) wake pattern as the "Coandă effect." The bulk flow leaks through the cylinder gap, staying attached to the convex cylinder surface, and entrains fluid from the surroundings, so that a region of lower pressure on the cylinder's circumference develops. However, it was later corrected that the "Coandă effect" was not the cause of the biased gap flow (with switching), as similar patterns were observed from two side-by-side prisms and flat plates - the convexity is a prerequisite to the "Coandă effect" (Miau et al., 1992, 1996; Bearman and Wadcock, 1973; Williamson, 1989). Thus far, no other plausible and convincing mechanism for the switching behavior of the gap flow between stationary side-by-side cylinders was provided.

In wind energy harvesting applications, a practical setup uses a short length-to-diameter ratio and a large cylinder-to-fluid mass ratio (m^* >> 1) (Wang et al., 2025), where either a single cylinder or both cylinders are flexibly mounted, and the motion of at least one cylinder is induced to enable the extraction of the associated kinetic energy. Similar to stationary side-by-side cylinders, an elastically mounted circular cylinder placed in close proximity to a stationary one also exhibits asymmetrical wake dynamics (i.e., bi-stable or tri-stable wakes). An important distinction was observed by Liu and Jaiman (Liu and Jaiman, 2016) and Huera-Huarte (Huera-Huarte, 2018), whereby the gap flow was stably deflected towards the vibrating cylinder as a stable event, i.e., no switching, as illustrated in Fig. 1(b). In their setups with low cylinder-fluid mass ratios (m^* ~ 10 (Liu and Jaiman, 2016) and 2.43 (Huera-Huarte, 2018) for a metallic cylinder submerged in water) at T/D = 1.6 (Liu and Jaiman, 2016) and T/D = 2.0 (Huera-Huarte, 2018), stably biased gap flow occurred together with a frequency lock-in process. Here, narrow wakes developed behind the vibrating cylinder, causing the vibration frequency of the flexible cylinder to match the narrow wake shedding frequency. However, there has

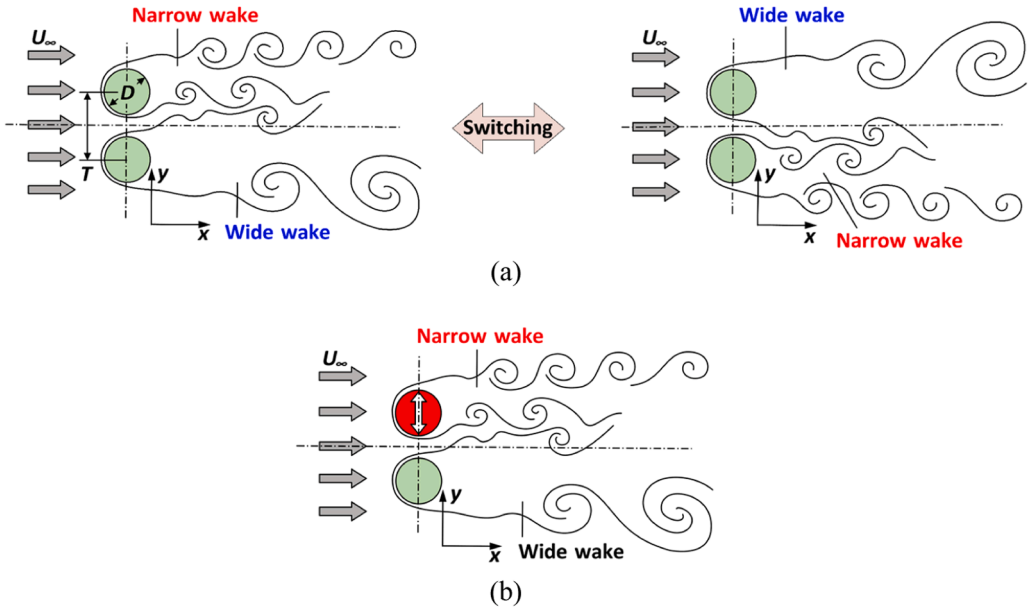

Fig. 1. Asymmetric wake patterns shed from side-by-side arranged cantilevers. (a) Wakes shed from two "stationary" cylindrical objects apart at 1.1~1.2 ≤ T/D ≤ 2.0~2.5 (Sumner et al., 1999; Zdravkovich 1988; Bearman and Wadcock, 1973; Sumner, 2010; Alam and Zhou, 2007; Wang and Zhou, 2005), adopted from Wang et al. (Wang et al., 2025). and (b) Wakes shed from a vibrating-stationary cantilever array, adopted and reproduced from Liu and Jaiman (Liu and Jaiman, 2016) at T/D = 1.5 and Huera-Huarte (Huera-Huarte, 2018) at T/D = 2.0.

been no plausible mechanism presented to explain how the stable asymmetric wake pattern is established, such that narrow wakes form only behind the vibrating cylinder while wide wakes are shed from the stationary cylinder, with no switching observed.

To elucidate on the fluid physics of stably biased gap flow developed behind an elastically mounted cylinder, a description of how wakes are shed from a circular cylinder in isolation is believed to be necessary. The most distinctive wake pattern formed behind an isolated cylinder is the "Kármán vortex street" or "Kármán vortices," featuring periodically shed vortex pairs that extend downstream as illustrated in Fig. 2 (Von Kármán, 1911; Williamson, 1996). In the subcritical Reynolds number range of 350~400 $\leq Re_D \leq$ 100,000~200,000, the transition from laminar to turbulent shear layers (TrSL) takes place in the near wake region (Zdravkovich, 1997), where undulations and small-scale vortices form along transitional separated shear layers that precede the Kármán vortices. This Reynolds number range is relevant to wind energy harvesting since the natural wind speed varies from 0.5 m/s to 10 m/s (Burton et al., 2011), corresponding to $Re_D = 700$ and $Re_D = 14{,}000$, respectively (if $D = 2.0$ cm as used in the present study).

Physical mechanisms underlying the "Kármán vortices" have long been a topic of research, with particular focus placed upon understanding how the shedding process evolves from a non-vortex shedding state, i.e., $Re_D = 49$ (Von Kármán, 1911; Williamson, 1996; Bénard, 1908; Nayler and Frazer, 1917; Zdravkovich, 1969). Specific to the subcritical Reynolds number regime characterized by TrSL, Gerrard (Gerrard, 1996) claimed that entrainment from the separated shear layer supplies a forming vortex on the opposite side and determines the shedding of mature Kármán vortices. Another account by Sumer and Fredsøe (Sumer and Fredsøe, 2006) is that the shedding of Kármán vortices occurs only when the two shear layers around a cylinder interact with each other. Thus, the separated shear layers from both sides of a cylinder and their subsequent interaction are defining characteristics of Kármán vortices.

The imbalance between the momentum of boundary layer flow and the adverse pressure gradient along the circumference of a cylinder causes the separation of a boundary layer (Schlichting and Gersten, 2017). In the TrSL regime, sinuous oscillation develops in the separated shear layers due to a susceptibility to instability caused by a velocity gradient that exhibits an inflection point in the shear layers, which has been referred to as the Kelvin–Helmholtz (K–H) mechanism (Bloor, 1964; Wei and Smith, 1986; Prasad and Williamson, 1997; Thompson and Hourigan, 2005). Thus, it is often termed a "K-H wave." The oscillation amplitude of the K-H wave increases with increasing Reynolds number (Zdravkovich, 1969), eventually developing into small-scale vortices (K-H vortices (Lin et al., 2002) with a specific spatial interval. These K-H vortices could be identified as a specific Reynolds number-dependent fluctuation frequency within the shear layers (Wei and Smith, 1986), and the associated Reynolds number scaling relation has been summarized (Prasad and Williamson, 1997; Thompson and Hourigan, 2005). It has been argued that K-H waves roll up into small vortices when $Re_D \geq 2000$ (Gerrard, 1996; Bloor, 1964; Wei and Smith, 1986; Gerrard, 1978; Kourta et al., 1987; Unal and Rockwell, 1988). In contrast to "large-scale" vortices, namely, the Kármán vortices, these small-scale K-H vortices can be scaled with the thickness of separated shear layers, which is generally a small fraction of the cylinder diameter. Therefore, the length and time scales of shear layer instability are much smaller than those associated with the instability of periodic Kármán vortex shedding (Prasad and Williamson, 1997). Accordingly, the frequency of the K-H vortices is much higher than that of the Kármán vortices. Furthermore, Unal and Rockwell (Unal

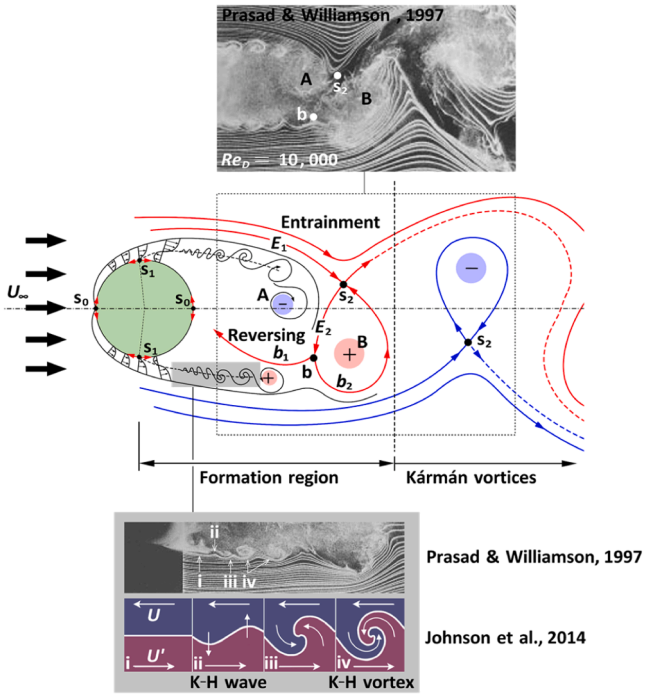

Fig. 2. Evolution of boundary layer separation from a circular object to Kármán vortices, at a subcritical Reynolds number regime characterized by the transition from laminar to turbulent shear layers (TrSL), where s_0: stagnation point and s_1: separation point, s_2: saddle point, and b_1: bifurcation point (Williamson, 1996; Zdravkovich, 1969; Gerrard, 1996; Bloor, 1964; Wei and Smith, 1986; Prasad and Williamson, 1997; Johnson et al., 2014).

and Rockwell, 1988) found that the K-H instability exhibits significant amplification at the 1/2-subharmonic of the naturally occurring shear layer frequency.

In summary, a boundary layer on each side of a cylinder is separated. Hereafter, it is termed a separated shear layer. With reference to the inset of Fig. 2 (from Johnson et al. (Johnson et al., 2014)), the K-H instability grows along the separated shear layer (i). Its growth is indicated by sinuous oscillation or undulation (ii), also called the "K-H waves," eventually followed by K-H vortices, i.e., small-scale vortices with a much higher convecting frequency. When a K-H vortex (denoted as Vortex "A" in Fig. 2) becomes strong enough, it entrains irrotational fluid from the outside of the upper shear layer (denoted as "Entrainment, "E_1" and "E_2" in Fig. 2). The entrained irrotational flow, E_2 cannot penetrate the lower shear layer (Gerrard, 1996). Thus, it instead bifurcates (indicated by point "b"). One such bifurcated stream towards the back surface of the cylinder forms "reverse flow, b_1", with eventual stagnation (s_0). This reverse flow acts to further strengthen Vortex A by feeding the same circulation. The other bifurcated stream "b_2" circulates around the last K-H vortex, which is formed along the other shear layer while feeding a fresh irrotational fluid, thus becoming stronger. As a result, the strengthened Vortex B developed in the lower shear layer becomes separated, and the circulating stream of Vortex B collides with the entrained flow, forming a "saddle point, s_2" (Nayler and Frazer, 1917; Perry et al., 1982) as shown in Fig. 2. Enhanced by this downward bifurcated flow leading to bifurcation point b, the fully developed Vortex B will eventually become strong enough to entrain fluid from the upper shear layer and, eventually, bifurcation point b vanishes. Thereafter, the strong Vortex B entrains fluid from the lower shear layer, causing upward entrainment into the formation region as a replenishment for the reversing flow during the next half cycle. Since the lower shear layer is not involved with Vortex B, it will supply fluid to the forming Vortex A and allow the cycle to repeat. Through the aforementioned process, the separated Vortex B from the serial K-H vortices becomes the first Kármán vortex.

Upon introducing an external acoustic excitation in the separated shear layers to force K-H instability, and thereby shorten the formation region of Kármán vortices (indicated in Fig. 2), Sheridan et al. (Sheridan et al., 1993) demonstrated the control of the

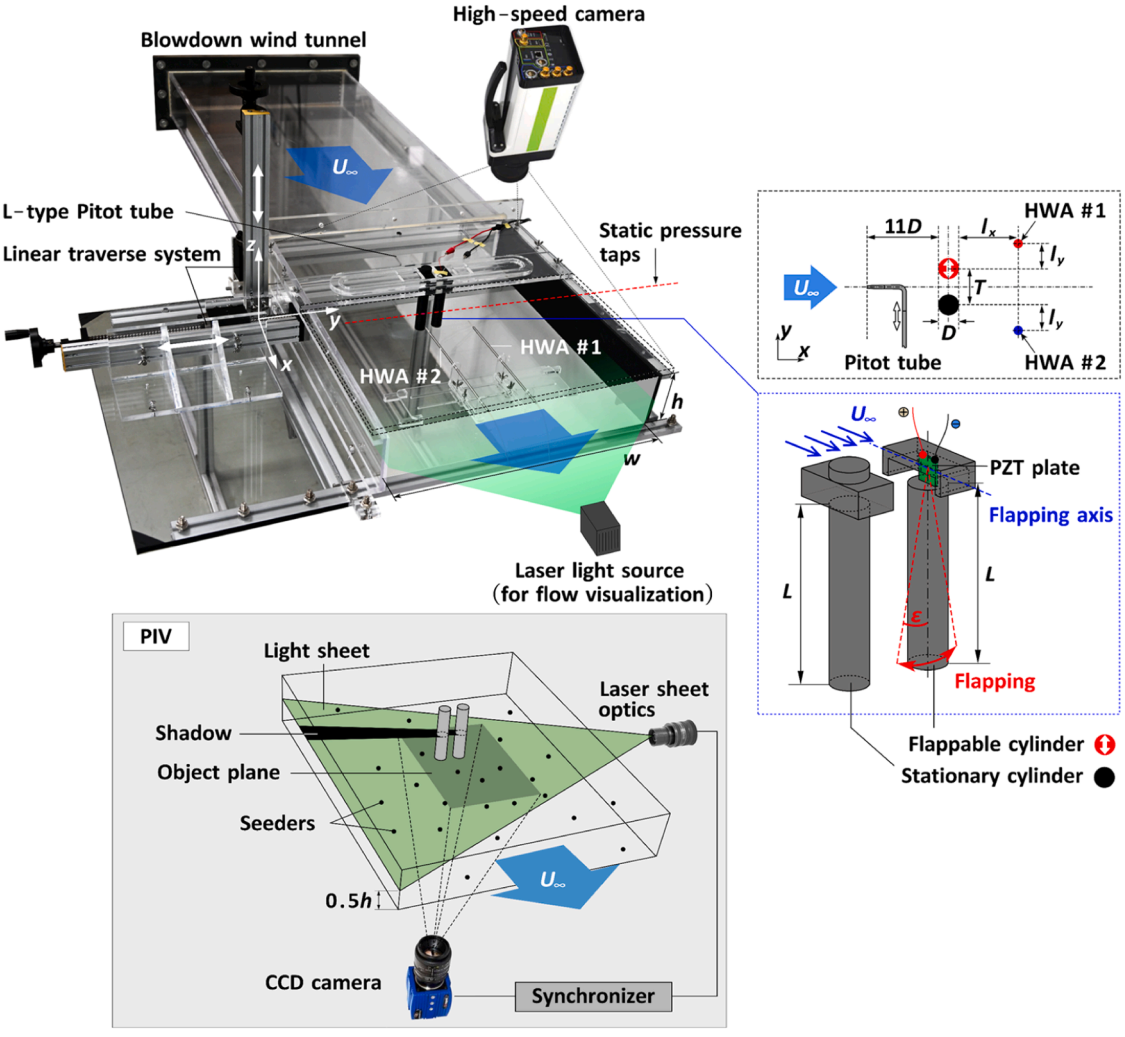

Fig. 3. Test setup: photograph and schematics showing a blowdown wind-tunnel and rectangular test section with two hot-wire anemometers (HWAs), particle image velocimetry (PIV), and a Pitot tube instrumented (Wang et al., 2025).

evolution process of Kármán vortices. Thus, we hypothesize that in a side-by-side flappable and stationary cantilever array, the flow-induced flapping motion acts to incite the forced K-H instability. Consequently, Kármán vortices that follow the K-H waves and K-H vortices along the separated shear layers are developed spatially earlier, thus altering the downstream wake-shedding characteristics. As a result, a certain flow property may trigger stably biased gap flow between these flapping and stationary cantilevers, with its effect being substantiated only in their close proximity.

To prove the hypothesis and stipulate the flow property that is altered due to the forced K-H instability by flapping, we carried out a series of experiments with a high cantilever-to-fluid mass ratio ($m^* \sim 1125$ for a polymer resin cylinder submerged in air). Flow visualization and spectral analysis of time-resolved data from hot-wire anemometers and the piezoelectric mount of a flapping cantilever were performed. In addition, particle image velocimetry was conducted to map instantaneous and time-averaged velocity and vorticity fields. During measurements, the center-to-center spacing normalized by a single cantilever diameter (T/D) – pitch ratio of side-by-side flappable and stationary cantilevers – was systematically varied in a Reynolds number range of $1800 \leq Re_D \leq 13{,}000$.

2. Experimental details

2.1. Test facility

A purposely designed test rig, consisting of a blowdown wind-tunnel and rectangular test section that accommodated stationary and flappable cantilevers, was constructed as shown in Fig. 3. The cantilever pair had an adjustable transverse center-to-center distance (T/D), while the wind-tunnel had a rectangular test section of $w = 480$ mm and $h = 100$ mm. Air at ambient conditions driven by a centrifugal blower of 7.5 kW passed through a set of grid meshes and honeycombs. A frequency inverter controlled the speed of airstream in the test section from $U_\infty = 1.0$ m/s to 13.5 m/s. Correspondingly, the Reynolds number based on a single cantilever's diameter $D = 20$ mm could be varied from 1500 to 16,000 (to be defined later). These Reynolds numbers fall within the regime of wake patterns transitioning along free shear layers (Wieselsberger, 1922) – termed here as the "transitional shear layer" (or TrSL) ($350 \sim 400 < Re_D < 100{,}000 \sim 200{,}000$): similar wake shedding patterns were thus expected.

The tested objects were mounted on the test section's upper wall. Both cantilevers had the diameter of $D = 20$ mm and a length of $L = 99$ mm. It follows that there was a 1.0 mm clearance gap for the cantilever's free end from the test section's lower wall. Both the stationary and flappable cantilevers were made of a photosensitive resin via 3D printing. The mounting of the flappable cantilever consisted of a flexible plate to allow "flapping" motion of the cylindrical rigid body, with respect to the flapping axis indicated in the inset of Fig. 3. The flexible mounting comprised of a lead zirconate titanate (PZT) ceramic bimorph plate (size of 20 mm × 8 mm × 0.8 mm), which was fixed to the base through the PZT plate with the length of $a = 8$ mm (i.e., the distance between the body and the base). As a key parameter of vortex-induced-vibration, the cantilever-to-fluid mass ratio was defined (Zdravkovich, 1985) as:

$$m^* = \frac{m}{\rho(D/2)^2} \tag{1}$$

where m is the per unit length mass of the cantilever immersed in the fluid (air), D is the cylinder diameter, and ρ is the fluid density. The calculated m^* of the tested flappable cantilever assemblies – the piezoelectric (PZT) plate and rigid cylinder – was 1125 with a natural frequency of 30 Hz and 31 Hz separately for flappable cylinder #1 and flappable cylinder #2; correspondingly, the damping was expressed as a logarithmic decrement of 0.017 and 0.016.

For the side-by-side arrangement, the center-to-center spacing (pitch ratio) of two parallel cantilevers was systematically (albeit manually) varied, as illustrated in Fig. 3. The flappable cantilever was free to flap without contacting the lower wall, generating piezoelectric voltage (V_p) signals that were connected to a data acquisition system (DL350, YOKOGAWA) at a sampling rate of 2.0 kHz. The acquired voltage signals allowed for spectral and phase analysis of the flapping cantilever's vibrational characteristics.

2.2. Time-averaged and time-resolved velocity measurements

To characterize the airflow interaction with the side-by-side cylinders time-averaged and time-resolved velocity measurements were taken using the experimental facility shown in Fig. 3. Further details of the experimental setup are provided in Wang et al. (Wang et al., 2025), where the freestream velocity profiles along the width (y-axis) and height (z-axis) of the test-section were measured $11D$ upstream, from the leading edge of both cantilevers, by a Pitot tube (L-type, 3.0 mm diameter) as shown in the inset of Fig. 3. Based on cantilever diameter D, the Reynolds number is defined as:

$$Re_D = \frac{\rho U_\infty D}{\mu} \tag{2}$$

where, ρ is the air density, U_∞ is the area averaged free stream velocity, and μ is the dynamic viscosity of air. Furthermore, the wake shedding patterns in the wind tunnel as the airflow interacts with the side-by-side cylinders were visualized using smoke-wire technique was used as described by Wang et al. (Wang et al., 2025).

To quantify the level of turbulence in the freestream by turbulence intensity (T_i), the time-resolved velocity was measured using a single velocity component hot-wire probe (5 μm in diameter; MiniCTA-54T42, Dantec Dynamics), at the same plane where time-averaged velocity was measured by the Pitot tube (Wang et al., 2025).

The frequency characteristics of the K-H waves, the K-H and the Kármán vortices in the shear layer and wakes of the stationary and

flappable cantilevers, time-resolved measurements were also carried out. For this purpose, two hot-wire anemometers (HWA #1 and #2) were used, with each positioned behind the test specimen at l_x along the x axis and l_y along the y axis from the trailing edge of both stationary and flappable cantilevers, as indicated by the inset of Fig. 3. The hot-wire signals were processed using a Fast Fourier Transformation (FFT) to convert discrete signals from the time domain to frequency domain, which enabled obtaining signal information about individual spectral components (frequency) and the corresponding energy distribution (power spectral density, PSD). As a result, dominant vortex shedding frequencies could be determined in the form of Strouhal number, defined as:

$$St = \frac{f_v D}{U_\infty} \tag{3}$$

where f_v is the dominant wake shedding frequency associated with PSD peaks in the power spectra of HWA signals, and D is the single cylinder diameter.

2.3. Velocity and vorticity field mappings

Downstream velocity and vorticity fields around the cantilevers, including the gap region, were mapped using particle image velocimetry (PIV). The PIV allowed both instantaneous and time-averaged flow properties to be mapped within the object plane (measurement area, as shown in Fig. 3. The laser source emitted a pulsed laser beam that was transformed into a laser sheet by the laser optics. Consequently, as shown in Fig. 3, laser illumination of the upstream and downstream wake regions for the pair of cylinders was achieved. The light-sheet thickness Δz was adjusted by the laser optics (i.e., $\Delta z \approx 1.0$ mm).

The flow field was seeded with an atomized mineral oil with a mean particle diameter of approximately 1 μm. The particles carried by the flow were then illuminated by a pulsed laser light sheet that had a 1.0 mm thickness. The green light sheet was generated from a frequency-doubled dual-cavity Nd: YAG laser (Evergreen 70, Lumibird), with a light wavelength of 532 nm. The light sheet was perpendicular to the center axis of the cantilevers and located at the midspan at $h/2$. The measurement period was defined by two sequential pulses of the laser light sheet that were separated by a finite time interval (7.65 μs).

The recorded flow field was represented by the random pattern of particle images captured by the image plane of the charge-coupled device (CCD) sensor. These images were recorded on the sensor frame that had a 2752 × 2200-pixel resolution. The field of view within the light sheet was denoted in Fig. 3 as an object plane, where the physical PIV measurement area was 168.1 × 134.4 mm, with a magnification factor of $M_0 = 0.15$. The optical axis of the camera was perpendicular to the laser light sheet, and the camera focused on the midspan plane of the cantilevers, which coincided with the light sheet. Acquisition of the velocity field depended upon estimating the displacement field, which was achieved based on the PIV images captured and interrogated using an integrated image acquisition and processing software (DaVis version 10.2.0, Lavision). The PIV images were divided into subregions (referred to as interrogation areas), which were 48 × 48 pixels in size and overlapped by 50 %. The obtained velocity field was further processed by converting to a fixed grid, via interpolation, to calculate the vorticity field. Subsequently, for a specific location in the flow field, both the velocity and vorticity fields were evaluated over an ensemble of 100 instantaneous maps that were sampled at a frequency of 12.75 Hz.

2.4. Static pressure measurements

The transverse variation of static pressure in the near wake of the cantilever array was measured by pneumatic pressure tappings. Fine steel tubes with an inner diameter of 0.6 mm were inserted into the top wall of the wind-tunnel test section, via drilled holes that were perpendicular to the wall surface, at a distance of 3.5 D downstream from the trailing edge of cantilevers (Fig. 3). Each tube was then connected to a differential pressure transducer (DSA3217, Scanivalve™), the latter sending data via a TCP/IP protocol to a data acquisition personal computer.

To evaluate pressure differences in the wakes of the two side-by-side arranged cantilevers, a non-dimensional pressure coefficient C_p was defined as:

$$C_p = \frac{p_{s1} - p_{s2}}{\rho U_\infty^2 / 2} \tag{4}$$

where p_{s1} and p_{s2} were the static pressures measured behind the cantilever #1 (stationary or flappable) and cantilever #2 (stationary), respectively.

2.5. Measurement uncertainties

Measurement uncertainties were estimated using a method detailed by Coleman and Steele (Coleman and Steele, 2018), as follows. If $y = f(x_1, x_2, \ldots, x_n)$, then the uncertainty propagated by x_i in the variable y is given by:

$$\Delta y = \sqrt{\left(\frac{\partial y}{\partial x_1}\Delta x_1\right)^2 + \left(\frac{\partial y}{\partial x_2}\Delta x_2\right)^2 + \cdots + \left(\frac{\partial y}{\partial x_n}\Delta x_n\right)^2} \tag{5}$$

where Δx_i is the absolute uncertainty in x_i. Eq. (5) was used in this study to estimate overall experimental uncertainties associated with

frequency and velocity measurements. The uncertainty associated with velocities measured by the Pitot tube and Reynolds number was calculated to be 1.64 %. Similarly, the uncertainty associated with voltage output was estimated to be 2.31 %. The measurement uncertainty of the Strouhal number was determined by that of the velocity and vortex shedding frequency and was estimated to be 4.3 %.

The instantaneous PIV velocity measurement uncertainty is primarily related to the estimation of the average particle displacement

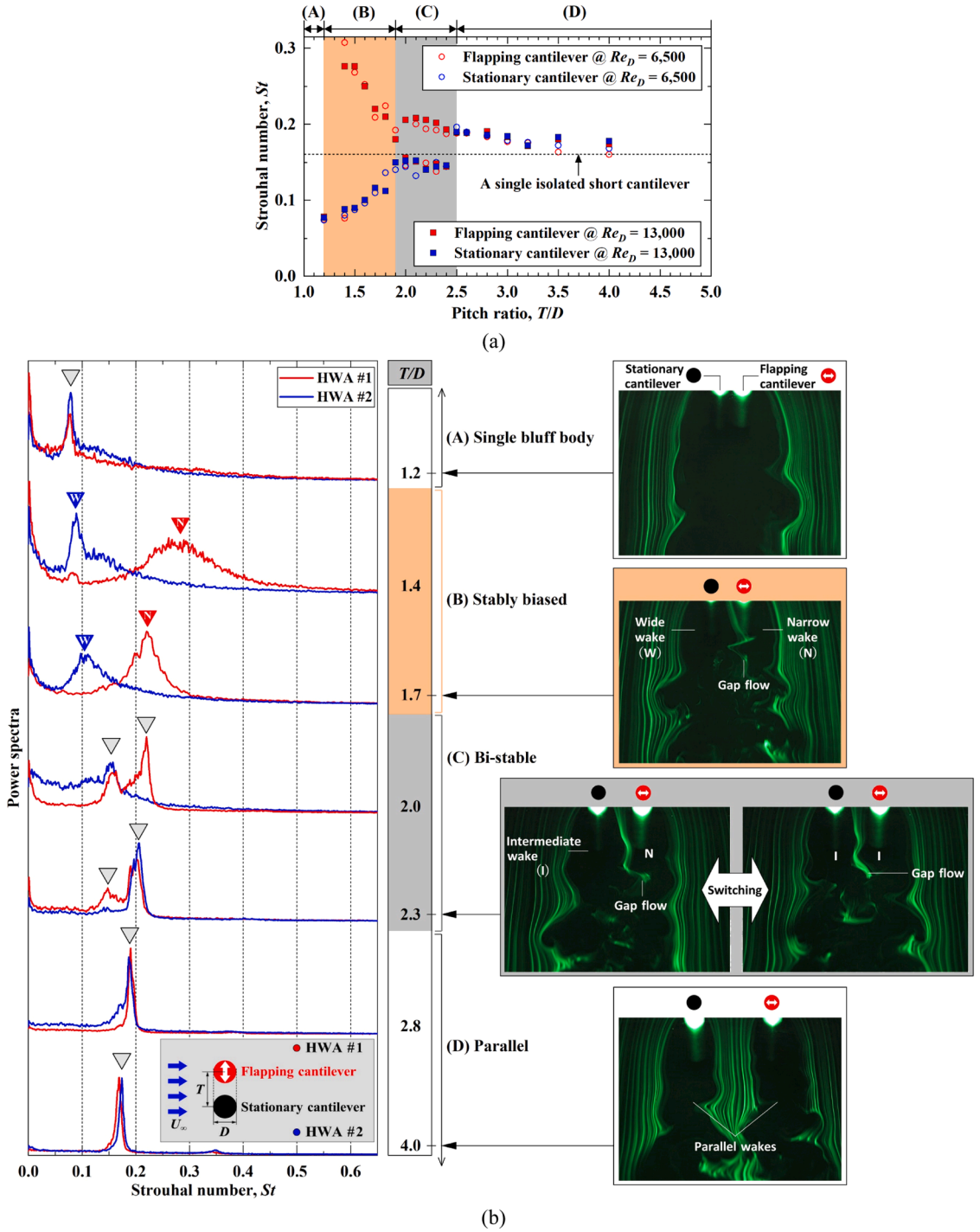

Fig. 4. Wakes shed from stationary-flapping cantilevers in a side-by-side arrangement. (a) Strouhal numbers (*St*) varying with pitch ratio (*T/D*) at two selected Reynolds numbers (Re_D = 6500 and 13,000), and (b) Power spectra of hot-wire anemometer signals (HWA #1 and HWA #2) at Re_D =13,000 (left) and visualized wake patterns, highlighting a gap flow behavior at selected pitch ratios for Re_D = 1800 (right).

within an interrogation area. The determination of measurement uncertainty relating to particle displacement was quantified analytically and by the generation of synthetic images with known parameter values (Westerweel, 1997, 2000; Adrian and Westerweel, 2010). A reasonable estimate of measurement error is given by Westerweel (Westerweel, 1997, 2000), which was applicable to the PIV algorithm used in this investigation. The total measurement error was estimated based on the contributions of the mean bias ($\varepsilon\Delta X$) and random errors ($\sigma\Delta X$) present during PIV interrogations. Westerweel (Westerweel, 1997, 2000) and Adrian and Westerweel (Adrian and Westerweel, 2010) showed that the random measurement errors are directly proportional to the particle image diameter (d_τ) and are a function of the number of particle images (NI) within the interrogation area, and sub-pixel displacements (ΔX). In addition, background noise contributes to the random error. Taking these factors into consideration the random error is estimated to be 0.17 pixels, based on an average particle image diameter of 2.8 pixels. The particle image diameter was measured using the auto-correlation of the PIV recordings, where the resulting self-correlation peak width is related to the particle image diameter as $d_\tau\sqrt{2}$. This method to determine the particle image diameter was preferred to the analytical diffraction-limited spot size estimation, which tends to underestimate the value of this parameter due to the non-ideal performance of the lens and imaging arrangement. The ideal number of particle image pairs (NI =10) for the displacement-correlation was assumed according to Adrian and Westerweel (Adrian and Westerweel, 2010). The bias error was estimated by Westerweel (Westerweel, 2000), which shows the error to be a function of the displacement correlation peak width. The present bias error was estimated to be 0.0066 pixels. Therefore, the total measurement uncertainty was determined to be 4.6 % based on the valid full-scale displacements of 1.2 pixels, where the total bias and random errors are combined by using the root-sum-square of these terms.

3. Results

Previous studies (Liu and Jaiman, 2016; Huera-Huarte, 2018) reported that the gap flow was stably biased towards the vibrating cylinder when the flow bled through the gap between two side-by-side stationary-elastically mounted cylinders. This stably biased gap flow (i.e., without switching) occurred for a water-stream when vortex shedding and vibration motion were locked-in (i.e., resonance), the cylinder-to-water mass ratio was low, and their center-to-center spacing was small (i.e., $T/D = 1.6$ & 2.0). Such stable and biased gap flow behavior is in contrast to the widely accepted bi-stable (or tri-stable) random switching of gap flow bled between two side-by-side stationary (Sumner et al., 1999; Kim and Durbin, 1988; Alam et al., 2003; Wang et al., 2025) or vibrating (Wang et al., 2025; Huera-Huarte, 2018) cylinder pair.

The setup of two side-by-side short stationary-flappable cantilevers immersed in an air-stream is like a vibrating elastic cylinder pair, practically relevant to wind energy harvesting. Here, the "flappability" of a short cantilever refers to flow-induced vibration of a rigid cantilever, with one end fixed to a bending flexible mount and the other end free to vibrate about a single "flapping axis." In this study, in the Reynolds number range of $1800 \leq Re_D \leq 13{,}000$, we demonstrated, for the first time, the wake shedding mechanism for flapping cylinders with varying center-to-center spacing, termed here as the "pitch ratio" (T/D). To this end, the characteristics of wake shedding including gap flow were analyzed using a dimensionless frequency, i.e., the Strouhal number (St, defined in Eq. (3)), at two selected Reynolds numbers ($Re_D = 6500$ and 13,000), with HWA probes positioned at $l_x = 3.5D$ and $l_y = 0.5D$ Fig. 4(a) presented four distinct wake regimes in the pitch ratio range of $1.2 \leq T/D \leq 4.0$, as: (A) Single bluff body wake regime, $1.0 < T/D \leq 1.2$; (B) Stably biased wake regime, $1.2 < T/D \leq 1.9$; (C) Bi-stable wake regime (i.e., biased wake regime with switching (also see, Fig. 4 for $T/D = 2.3$), $1.9 < T/D \leq 2.4$; (D) Parallel wake regime, $2.4 < T/D$. This classification is somewhat similar to that of two side-by-side stationary cantilevers and two side-by-side flapping, short cantilevers (Wang et al., 2025). However, one distinction is that, for relatively small pitch ratios (e.g., $1.2 < T/D \leq 1.9$), the shed wakes are stably biased towards the flapping cantilever, rather than exhibiting bi- or tri-stability.

In the single bluff body wake regime (A), i.e., $T/D \sim 1.2$, a single Strouhal number (St) existed; Fig. 4(b). The power spectra of two HWA signals showed the same Strouhal number peak at $St \sim 0.076$, based on cantilever diameter D. Corresponding flow visualization image showed a large-scale single wake formed behind the two side-by-side stationary-flapping short cantilevers, which were shed from the outer sides of the cylinders. The influence of gap flow on the overall wake pattern was small. Consequently, the two cantilevers in close proximity behaved like a single bluff body having an equivalent diameter of $D_e = 2D$, giving rise to 2 St $\sim$ 0.16, which is the Strouhal number associated with a single cantilever of diameter D_e in isolation. As the cylinders tested in the current study were relatively short, this Strouhal number is slightly lower than that of "long" circular stationary cylinders (Kamemoto, 1976; Okamoto and Yagita, 1973; Rooney et al., 1995).

Fig. 4(b) showed flow visualization where the gap flow had a *stably biased* deflection towards the vibrating cylinder, with the switching behavior cancelled out. For example, when $T/D = 1.7$, low and high Strouhal numbers were separately observed in the wakes of the stationary and the vibrating cylinders: thus, for a given pitch ratio within $1.2 < T/D \leq 1.9$, the biased wake regime was classified as (B) in Fig. 4(a). The gap flow was biased towards the flapping cantilever, and no switching was involved, evidenced by the power spectra. Both the flow visualization image and spectral signals showed that the high St coincided with the narrow wake (denoted by "N"), formed behind the flapping cantilever, whereas the low St indicated the wide wake (denoted by "W") shed from the stationary cantilever. In addition, the HWA signal behind each cantilever exhibited only a single dominant shedding frequency, thus confirming the stably biased wake behavior. As the pitch ratio was increased towards $T/D = 1.9$, the low St increased to approach $St = 0.16$, which was equivalent to that of a single cantilever in isolation. On the other hand, the high St decreased, approaching a value of $St \sim 0.2$ (Fig. 4(a)). This wake regime was unique to the present particular setup of two side-by-side short stationary-flapping cantilevers immersed in air-stream.

As the pitch ratio was further increased to fall in the range of $1.9 < T/D \leq 2.4$, the bi-stable wake regime (C) was formed (Fig. 4(a)). In contrast to the stably biased wake region (B), the HWA signal behind each cantilever for the bi-stable wake regime (C) exhibited two

dominant shedding frequency peaks, thus confirming the bi-stable or switching wake behavior. Here, the intermittent, random switching for the bi-stable wake regime (C) was shown with flow visualization, whereby the gap flow deflection might either be directed towards the stationary or the vibrating (flapping) cylinder. The power spectral data of Fig. 4(b) indicated that the wake shedding frequency for the narrow wake (N) was $St \sim 0.2$ and, for the wide wake (W), $St \sim 0.16$. The wide wake St is coincident with that of a single isolated short cantilever (diameter D) as indicated by the dotted line at $St = 0.16$ in Fig. 4(a).

Lastly, for a large pitch ratio, i.e., $T/D > 2.4$, the parallel wake regime (D) was displayed. The gap between the side-by-side cantilevers ($= T - D$) was wide enough so that the gap flow behaved like a freestream passing around the two separate cantilevers. From flow visualization, both in-phase and anti-phase wake patterns developed, which demonstrated coupling despite the greater gap spacing. At $T/D = 2.5$, the St of the wide wake suddenly merged to the narrow wake St (Fig. 4(a)). As the pitch ratio increased further, the St gradually decreased, eventually approaching $St = 0.16$, which is equivalent to that of a single short cantilever in isolation (Wang et al., 2025).

In summary, the *stably biased* gap flow was unique to the setup of two side-by-side short ($1.2 < T/D \leq 1.9$) stationary-flapping cantilevers immersed in air-stream, rather than the bi - or tri-stability observed in the two side-by-side arrangement of either stationary or flapping cantilevers (Sumner et al., 1999; Kim and Durbin, 1988; Alam et al., 2003; Wang et al., 2025). However, the physical mechanism underpinning the stably biased gap flow behavior is essentially obscure.

Flow visualization of wake pattern with $Re_D = 1800$ and $T/D = 1.7$ was presented in Fig. 5(a). A wide wake was formed behind the stationary cantilever, while narrow wakes convected downstream from the flapping cantilever. The separated shear layers on the flapping cantilever side evolved to a series of vortices smaller than those on the stationary cantilever side. More importantly, flow that was bled through the gap of $T - D = 0.7D$ (or $T/D = 1.7$) was biased towards the flapping cantilever. To provide improved insight into how these vortices were formed behind each cantilever, the vorticity (ω_z) was introduced, which was defined as:

$$\omega_z = \frac{dU_y}{dx} - \frac{dU_x}{dy} \tag{6}$$

where U_x and U_y are the x- and y-velocity components at an arbitrary point, respectively. The vorticity was then mapped with the technique of PIV. In Fig. 5(b), the results of an instantaneous vorticity contour map at $T/D = 1.7$ and $Re_D = 13{,}000$ demonstrated that small-scale K-H vortices developed in the shear layers. Note that, immediately downstream of both cantilevers, serially separated

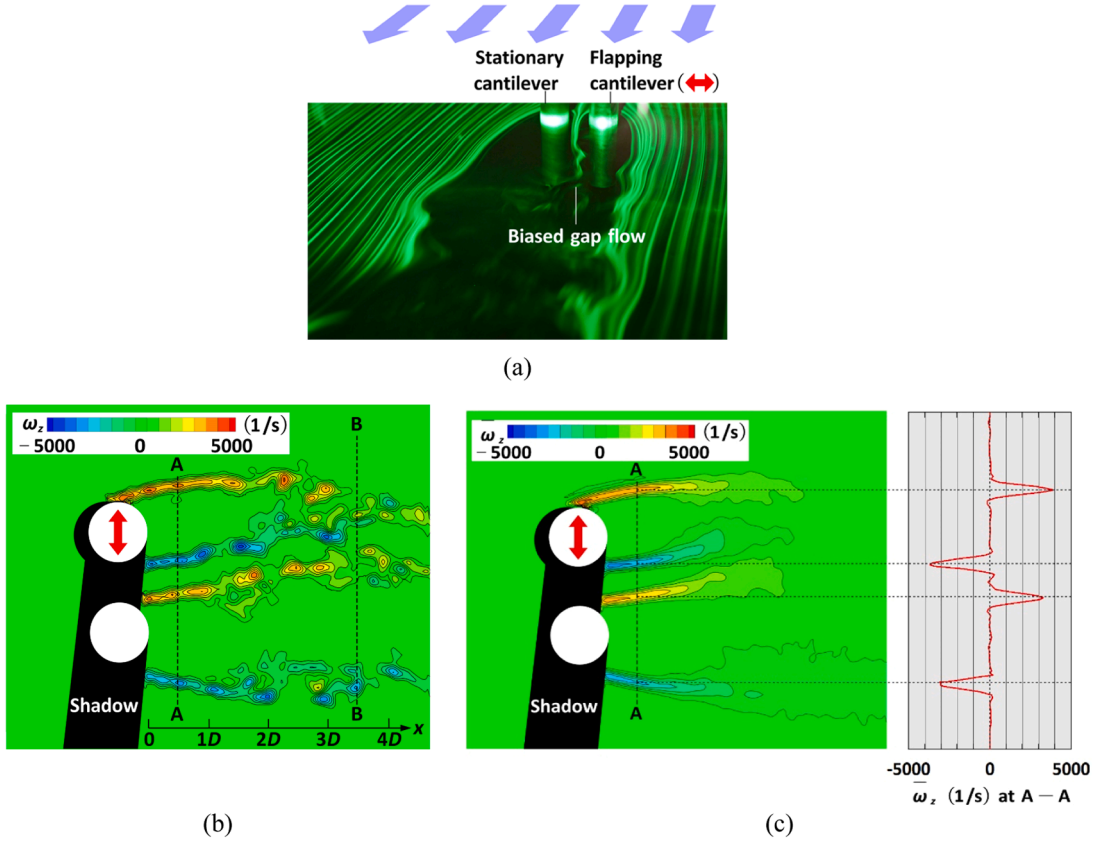

Fig. 5. Stably biased gap flow and shear layers developed above the flapping cantilever at $Re_D = 13{,}000$ and $T/D = 1.7$. (a) Visualized stably biased gape flow, (b) Instantaneous vorticity (ω_z) distribution by PIV, and (c) Time-averaged vorticity ($\overline{\omega}_z$) distribution over 100 PIV images in 30.15 s.

islands of concentrated vorticity formed along the shear layers, revealing undulating vorticity. At a certain downstream location, the isolated concentrations of vorticity evolved into large-scale vortices, conventionally known as the "Kármán vortices." The detailed evolution sequence of these large vortices could be referred to Fig. 2.

In the present setup, the K-H vortices eventually grow to form larger-scale Kármán vortices at about 3*D* downstream. From Figs. 5 (b, c), it could be seen that the vorticity along the shear layers shed from the flapping cantilever was stronger than that from the stationary cantilever. Although the time-averaging of instantaneous vorticities blurred the details (Fig. 5(c)), it still indicated stronger vorticity and longer shear layers corresponding to the flapping cantilever side. The time-averaged vorticities extracted along A-A in Fig. 5(c) quantitatively confirmed that, at a given downstream plane before the Kármán vortices, the vorticity developed from the flapping cantilever was stronger (i.e., $\omega_{s\,\max} = 4955\ s^{-1}$) than that from the stationary one (i.e., $\omega_{s\,\max} = -3915\ s^{-1}$).

To explore fluid mechanisms underpinning the strengthened vorticity due to flapping as evidenced in Fig. 5, Fig. 6 shows the results of power spectral analysis for $Re_D = 13{,}000$. The Fast Fourier Transformation (FFT) of the velocity signals measured with hot wire anemometers (HWAs) provided insight into dominant vortex shedding and K-H frequencies in the shear layers. Downstream of the two cantilevers in the upper shear layer of each cantilever, the HWAs were positioned at $l_x = 0.5D$, $l_y = 0.5D$, denoted as A-A in Figs. 5 (b, c), and $l_x = 3.5D$, $l_y = 0.5D$, denoted as B-B in Fig. 5(b).

Firstly, to establish a reference case and eliminate any interference from neighboring flapping or stationary cantilever, velocity signals of the HWA at $l_x = 0.5D$ for an isolated stationary cantilever and an isolated flapping cantilever were compared in Fig. 6(a). The total power of velocity signals was calculated by integrating the power spectral density (PSD) magnitude over the entire frequency range. Thus, the intensity of a specific periodic behavior reflected by signal fluctuations was determined by the PSD's magnitude.

The large-scale Kármán vortices were consistently represented by a dominant frequency peak at $f_v = 75$ Hz, giving rise to a corresponding Strouhal number of $St = f_v D/U_\infty = 0.16$ for either a stationary or flapping short ($L/D = 5.0$) cantilever in isolation. In contrast, small-scale K-H vortices developed at higher frequencies (Bloor, 1964; Prasad and Williamson, 1997). Prasad and Williamson (Prasad and Williamson, 1997) proposed an empirical correlation in the form of $f_{K\text{-}H} = f_v(Re_D/262)^{0.67}$, $f_{K\text{-}H}$ and f_v being the frequency of K-H vortices and Kármán vortices, respectively. Based on the present data of $f_v = 75$ Hz, this formula predicted $f_{K\text{-}H} = 1025$ Hz, which coincided well with the peak of $f_{K\text{-}H} = 1050$ in Fig. 6(a). Half of the K-H vortex shedding frequency (i.e., $f_{K\text{-}H}/2$) was also identified, since it is associated with the occurrence of vortex pairing shed from both sides (Kourta et al., 1987; Khabbouchi et al., 2014; Mi et al., 2011). For both cases, $f_{K\text{-}H}/2$ was captured by another peak, also shown in Fig. 6(a). For an isolated flapping or stationary cantilever, it became clear that f_v and $f_{K\text{-}H}$ had the same frequency distributions, but flapping enlarged the PSD magnitude.

At $Re_D = 13{,}000$, consider next the case of stationary-flapping cantilevers with $T/D = 1.7$. With reference to Fig. 4, the stably biased gap flow featured a wide wake formed only behind the stationary cantilever and a narrow wake shed from the flapping cantilever. On the stationary side, the peak frequency measured at the $l_x = 3.5D$ (B-B) downstream plane indicated that the Karman vortex shed at $f_{vW} = 55$ Hz corresponded to the wide wake. Other peaks were also captured at 600 Hz and 300 Hz, which indicated the K-H vortices and their pairing, respectively. It should be pointed out that these higher frequencies were measured at the $l_x = 0.5D$ (A-A) downstream plane. On the other hand, behind the flapping cantilever, the peak frequency associated with the Karman vortices was measured to be $f_{vN} = 115$ Hz (representing the narrow wake), while the other two high frequencies were $f_{K\text{-}H} = 600$ Hz and $f_{K\text{-}H}/2 = 300$ Hz, consistent with those obtained for the stationary cantilever. Only the magnitude of PSD was increased.

In summary, the shedding of K-H vortices from both stationary and flapping cantilevers occurred at the same frequencies. However, the power concentration differed: the flapping caused a stronger PSD in both the K-H vortices and Kármán vortices. Since K-H instability preceded these vortices, it might be concluded that the flapping intensified K-H waves, thus facilitating their evolution to K-H vortices along the shear layers.

It appeared that the intensified K-H vortices spatially evolved to Kármán vortices, as shown by the contours of instantaneous vorticity (Fig. 5(b)) and velocity (Fig. 7(a)) mapped via PIV measurements. Furthermore, downstream of the cylinder, the pairs of Kármán vortices emerged sooner in the near wake. As a result, the velocity deficit caused by the narrow wake was recovered sooner than that by the wide wake. The contour of time-averaged velocity in Fig. 7(b) clearly depicted a faster velocity recovery behind the flapping cantilever, enabling a transverse pressure gradient to form. Here, static pressure was measured in the near wake using 15 flush

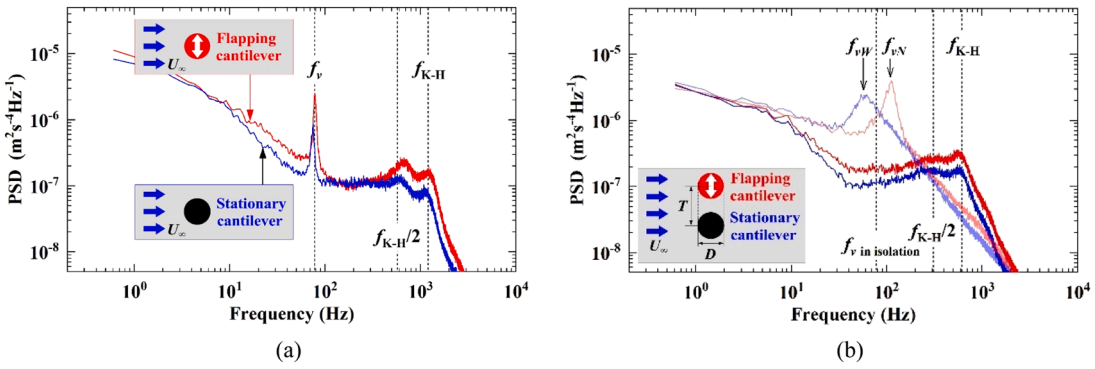

Fig. 6. Power spectral density (PSD) of near-wake velocity fluctuation behind cantilevers at $Re_D = 13{,}000$. (a) Stationary cantilever and flapping cantilever, each in isolation, and (b) Flapping-stationary cantilevers at $T/D = 1.7$.

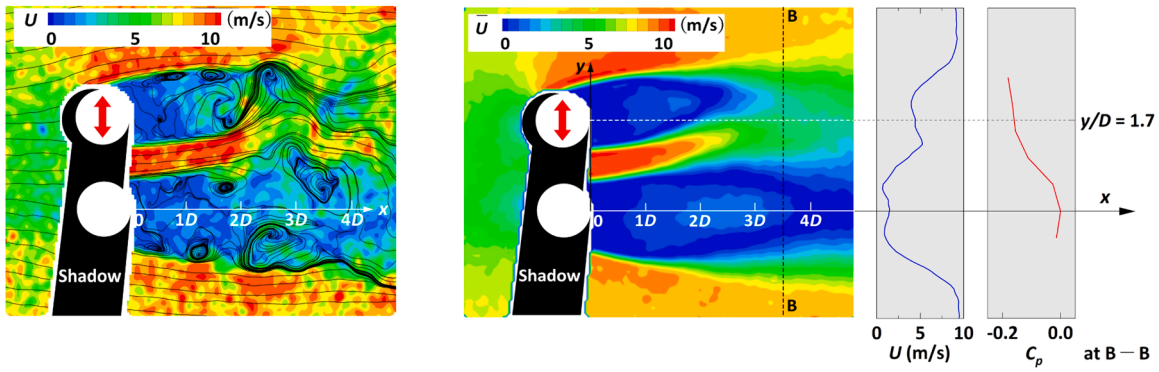

Fig. 7. Velocity field behind flapping-stationary cantilevers in a side-by-side arrangement at $Re_D = 13,000$ and $T/D = 1.7$ by PIV. (a) Instantaneous velocity field (U), and (b) Time-averaged velocity ($\overline{U}$) field and transverse distributions of $\overline{U}$ and C_p at a 3.5D downstream plane (B-B).

mounted pressure tappings distributed along the B-B line (at the 3.5D downstream plane, measured from the trailing edge of each cantilever). The measured distribution of transverse static pressure indicated that the narrow wake had a lower pressure than the wide wake, suggesting that a transverse pressure gradient was established in the near wake. In turn, the transverse pressure gradient pushed the gap flow towards the flapping cantilever, thus creating the observed *stably biased* gap flow.

We have now claimed that the downstream pressure gradient acting transversely (and its upstream penetration as a potential effect) is responsible for the stably biased gap flow, based on pressure and velocity data obtained at $T/D = 1.7$. In the present setup, the biased wake regime existed in a range of $1.2 < T/D < 1.9$, as seen in Fig. 4. Therefore, we need to confirm that the claimed cause still holds for other pitch ratios within the regime. To this end, static pressures were measured using two pressure tappings aligned with both cantilever axes, positioned at 3.5D downstream each cantilever. The obtained results were presented in the form of a pressure coefficient C_p, defined in Eq. (6). This pressure coefficient indicated the magnitude of transverse pressure difference that existed between the two cantilevers while the pitch ratio was varied.

As a reference, the difference of transverse pressure (p_{s1} - p_{s2}) measured in the near wake of two stationary cantilevers was firstly presented in Fig. 8(a). For a given pitch ratio in the entire range considered (i.e., $1.2 \leq T/D \leq 4.0$), the pressure difference fluctuated with respect to a zero difference ($C_p = 0$), leading to the previously observed tri-stable or bi-stable gap flow with random switching

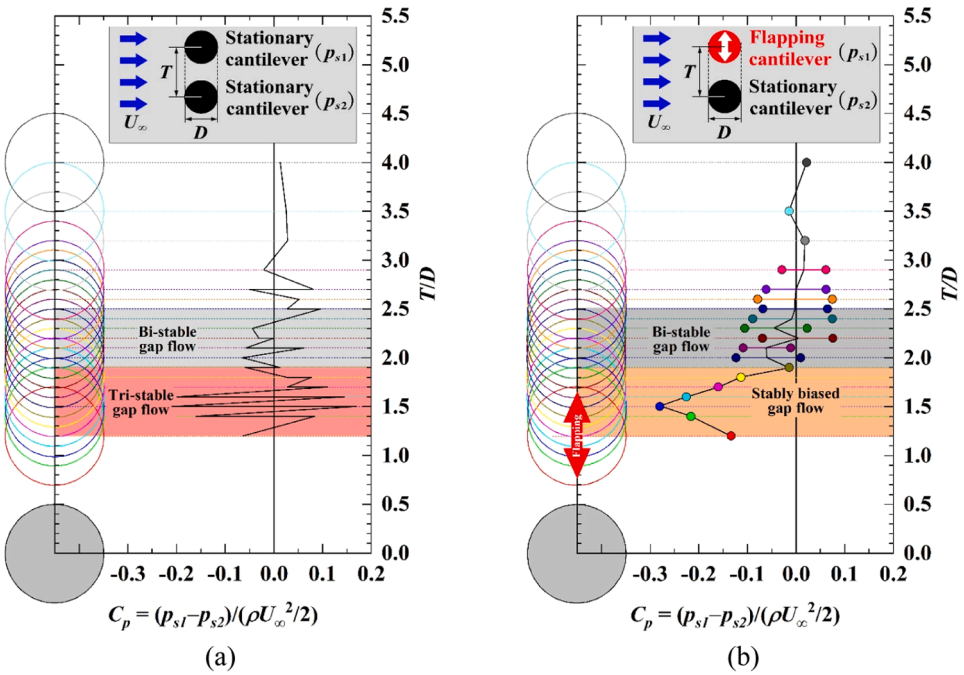

Fig. 8. Downstream pressure difference of the two side-by-side cantilevers at $x/D = 3.5$ (along B-B indicated in Fig. 7(b)) with a varying center-to-center distance at $Re_D = 13,000$ and $T/D = 1.7$. (a) Two stationary cantilevers as reference, and (b) Flapping-stationary cantilevers.

(Kim and Durbin, 1988). In sharp contrast, with a flapping cantilever set next to the stationary cantilever in a side-by-side manner (Fig. 8(b)), a stable, negative pressure difference existed in $1.2 < T/D < 1.9$. It followed that a higher pressure was present behind the stationary cantilever, instead of the flapping one. At $T/D \geq 1.9$, the pressure coefficient C_p began to fluctuate with respect to zero C_p difference, causing the bi-stable gap flow switching behavior to appear again. Thus, Fig. 8(b) demonstrated that, only within the pitch ratio range of $1.2 < T/D < 1.9$, the formation of stable transverse pressure gradients in the near wake was responsible for the stably biased gap flow.

4. Conclusions

When a stationary cylinder is placed side-by-side with a flapping cylinder, the gap flow between them was previously observed to be stably biased towards the flapping cylinder, yet the mechanism underpinning this fluidic behavior remained largely obscure. This study squarely investigated a plausible mechanism for the stably biased gap flow behavior, which is relevant for wind energy harvesting in which the cantilever-to-fluid mass ratio is large. Flow visualization and spectral analysis of time-resolved data from hot-wire anemometers and the piezoelectric mount of a flapping cantilever were carried out. Particle image velocimetry was also conducted to map the instantaneous and time-averaged velocity fields. We demonstrated, for the first time, how wakes were shed in this particular setup within the Reynolds number range of $1800 \leq Re_D \leq 13{,}000$, with the center-to-center distance T/D (pitch ratio) systematically varied. The stably biased gap flow occurred only in the pitch ratio range of $1.2 < T/D \leq 1.9$, where no switching occurred. Flapping intensified the Kelvin-Helmholtz (K-H) instability along shear layers separated from the flapping cantilever, leading to a longitudinally earlier evolution into the K-H waves and K-H vortices. Thus, the earlier onset of Kármán vortices was triggered. As a result, the velocity deficit caused by the narrow wake was recovered longitudinally earlier than that by the wide wake, resulting in a transverse pressure gradient acting towards the flapping cantilever as well as its upstream penetration due to potential effect. Consequently, the gap flow was stably pushed towards the flapping cantilever as observed.

CRediT authorship contribution statement

Yongpu Wang: Writing – review & editing, Writing – original draft, Resources, Methodology, Investigation, Data curation, Conceptualization. **Yanyan Liu:** Writing – review & editing, Validation, Methodology, Funding acquisition. **Michael David Atkins:** Writing – review & editing, Supervision. **Tian Jian Lu:** Writing – review & editing, Supervision, Funding acquisition. **Tongbeum Kim:** Validation, Writing – review & editing, Writing – original draft, Supervision, Project administration, Methodology, Funding acquisition, Formal analysis, Conceptualization.

Declaration of competing interest

The authors declare that they have no known competing financial interests or personal relationships that could have appeared to influence the work reported in this paper.

Acknowledgments

This work was supported partially by the Double Innovation Talent Foundation of Jiangsu Province, China (JSSCRC2021502) and the Double Innovation Team Foundation of Jiangsu Province, China (JSSCTD202206).

T.K. conceived the idea. T.J.L. and T.K. secured the funding. Y.W. and Y.L. designed the experiment and measurements. Y.W., M.D.A. and T.K. performed the data analysis. Y.W., M.D.A., T.J.L., and T.K. wrote the manuscript. M.D.A. T.J.L., and T.K. revised the manuscript.

Data availability

Data will be made available on request.

References

Adrian, R.J., Westerweel, J., 2010. Particle Image Velocimetry. Cambridge University Press, Cambridge. ISBN: 978-0-521-44008-0.

Alam, M.M., Moriya, M., Sakamoto, H., 2003. Aerodynamic characteristics of two side-by-side circular cylinders and application of wavelet analysis on the switching phenomenon. J. Fluids Struct. 18 (3–4), 325–346. https://doi.org/10.1016/j.jfluidstructs.2003.07.005.

Alam, M.M., Zhou, Y., 2007. Flow around two side-by-side closely spaced circular cylinders. J. Fluids Struct. 23 (5), 799–805. https://doi.org/10.1016/j.jfluidstructs.2006.12.002.

Atkins, M.D., Dala, L., Kim, T., 2016. Time-averaged behavior of gap flow between two side-by-side circular cylinders. AIAA J 54, 9. https://doi.org/10.2514/1.j054638.

Bearman, P.W., Wadcock, A.J., 1973. The interaction between a pair of circular cylinders normal to a stream. J. Fluid Mech. 61 (3), 499–511. https://doi.org/10.1017/s0022112073000832.

Bénard, H., 1908. Formation périodique de centres de giration à l'arrière d'un obstacle en mouvement. Comp. Rend. Paris 147, 839–842.

Bloor, M.S., 1964. The transition to turbulence in the wake of a circular cylinder. J. Fluid Mech. 19, 209. https://doi.org/10.1017/s0022112064000726.

Brun, C., Tenchine, D., Hopfinger, E.J., 2004. Role of the shear layer instability in the near wake behavior of two side-by-side circular cylinders. Exp. Fluid. 36, 334–343. https://doi.org/10.1007/s00348-003-0726-6.

Burton, T., Jenkins, N., Sharpe, D., Bossanyi, E., 2011. Wind Energy Handbook. John Wiley & Sons, Hoboken, New Jersey. https://doi.org/10.1002/9781119992714.

Coleman, H.W., Steele, W.G., 2018. Experimentation, validation, and Uncertainty Analysis For Engineers. John Wiley & Sons, Hoboken, New Jersey. https://doi.org/10.1002/9781119417989.
Gerrard, J.H., 1978. The wakes of cylindrical bluff bodies at low Reynolds number. Philosophic. Transac. Royal Soc. London. Series A, Mathematic. Physic. Scienc. 288 (1354), 351–382. https://doi.org/10.1016/j.oceaneng.2019.04.093.
Gerrard, J.H., 1996. The mechanics of the formation region of vortices behind bluff bodies. J. Fluid Mech. 25 (2), 401–413. https://doi.org/10.1017/s0022112066001721.
Huera-Huarte, F.J., 2018. Dynamics and excitation in a low mass-damping cylinder in cross-flow with side-by-side interference. J. Fluid Mech. 850, 370–400. https://doi.org/10.1017/jfm.2018.469.
Ishigai, S., Nishikawa, E., Nishimura, E., Cho, K., 1972. Experimental study of structure of gas flow in tube banks axes normal to flow. Bullet. Japan Soc. Mechanic. Eng. 15, 949–956. https://doi.org/10.1299/jsme1958.15.949.
Johnson, J.R., Wing, S., Delamere, P.A., 2014. Kelvin Helmholtz instability in planetary magnetospheres. 184, 1–31. DOI: 10.1007/s11214-014-0085-z.
Kamemoto, K., 1976. Formation and interaction of two parallel vortex streets. Bullet. JSME. 19 (129), 283–290. https://doi.org/10.1299/jsme1958.19.283.
Khabbouchi, I., Fellouah, H., Ferchichi, M., Guellouz, M.S., 2014. Effects of free-stream turbulence and reynolds number on the separated shear layer from a circular cylinder. J. Wind Eng. Ind. Aerodyn. 135, 46–56. https://doi.org/10.1016/j.jweia.2014.10.005.
Kim, H.J., Durbin, P.A., 1988. Investigation of the flow between a pair of circular cylinders in the flopping regime. J. Fluid Mech. 196, 431–448. https://doi.org/10.1017/s0022112073000832.
Kourta, A., Boisson, H.C., Chassing, P., Haminh, H., 1987. Nonlinear interaction and the transition to turbulence in the wake of a circular cylinder. J. Fluid Mech. 181, 141–161. https://doi.org/10.1017/s0022112087002039.
Lee, Y.J., Qi, Y., Zhou, G., Kim, B.L., 2019. Vortex-indued vibration wind energy harvesting by piezoelectric MEMS device in formation. Sci., Rep 9, 20404. https://doi.org/10.1038/s41598-019-56786-0.
Lin, J.-C., Yang, Y., Rockwell, D., 2002. Flow past two cylinders in tandem instantaneous and averaged flow structure. J. Fluid. Struct. 16 (8), 1059–1071. https://doi.org/10.1006/jfls.2002.0469.
Liu, B., Jaiman, R.K., 2016. Interaction dynamics of gap flow with vortex-induced vibration in side-by-side cylinder arrangement. Phys. Fluid. 28, 127103. https://doi.org/10.1063/1.4968587.
Mi, J., Xu, M., Antonia, R.A., Wang, J.J., 2011. Thermal characteristics of the wake shear layers from a slightly heated circular cylinder. Exp Fluid 50, 429–441. https://doi.org/10.1007/s00348-010-0944-7.
Miau, J.J., Wang, G.Y., Chou, J.H., 1992. Intermittent switching of gap flow downstream of two flat plates arranged side by side. J. Fluid Struct. 6, 563–582. https://doi.org/10.1016/0889-9746(92)90019-y.
Miau, J.J., Wang, H.B., Chou, J.H., 1996. Flopping phenomenon of flow behind two plates placed side-by-side normal to the flow direction. Fluid Dyn. Res. 17, 311–328. https://doi.org/10.1016/0169-5983(95)00034-8.
Nayler, J.L., Frazer, R.A., 1917. Vortex motion. (i) Preliminary report upon an experimental method of investigating, by the aid of kinematograph photography, the history of eddying flow past a model immersed in water. Aeronaut. Res. Coun. Rep. Memo. 332.
Okamoto, T., Yagita, M., 1973. The experimental investigation on the flow past a circular cylinder of finite length placed normal to the plane surface in a uniform stream. Bullet. JSME 16 (95), 805–914. https://doi.org/10.1299/jsme1958.16.805.
Perry, A.E., Chong, M.S., Lim, T.T., 1982. The vortex-shedding process behind two-dimensional bluff bodies. Space Sci. Rev. 116, 77–90. https://doi.org/10.1017/s0022112082000378.
Prasad, A., Williamson, C.H.K., 1997. The instability of the shear layer separating from a bluff body. J. Fluid Mech. 333, 375–402. https://doi.org/10.1017/s0022112096004326.
Rooney, D.M., Rodichok, J., Dolan, K., 1995. Finite aspect ratio effects on vortex shedding behind two cylinders at angles of incidence. J. Fluid Eng. 117 (2), 219–226. https://doi.org/10.1115/1.2817133.
Schlichting, H., Gersten, K., 2017. Boundary-layer Theory, 9th edition. Springer, Berlin Heidelberg. https://doi.org/10.1007/978-3-662-52919-5. 2017.
Sheridan, J., Soria, J., Jie, W., Welsh, M.C., 1993. The Kelvin-Helmholtz instability of the separated shear layer from a circular cylinder. In: Eckelmann, H., Graham, J. M.R., Huerre, P., Monkewitz, P.A. (Eds.), Bluff-body wakes, Dynamics and Instabilities. Springer, Berlin, Heidelberg, pp. 115–118. https://doi.org/10.1007/978-3-662-00414-2_27.
Sumer, B.M., Fredsøe, J., 2006. Hydrodynamics Around Cylindrical Structures - advanced series On Coastal Engineering, 12. World Scientific, River Edge, New Jersey. https://doi.org/10.1142/6248.
Sumner, D., 2010. Two circular cylinders in cross-flow: a review. J. Fluids Struct. 26 (6), 849–899. https://doi.org/10.1016/j.jfluidstructs.2010.07.001.
Sumner, D., Wong, S.S., Price, S.J., Païdoussis, M.P., 1999. Fluid behavior of side-by-side circular cylinders in steady cross-flow. J. Fluids Struct. 13 (3), 309–338. https://doi.org/10.1006/jfls.1999.0205.
Thompson, M.C., Hourigan, K., 2005. The shear-layer instability of a circular cylinder wake. Phys. Fluid. 17, 021702. https://doi.org/10.1063/1.1852581.
Unal, M.F., Rockwell, D., 1988. On the vortex formation from a cylinder. Part 1. The initial instability. J. Fluid Mech. 190, 491–512. https://doi.org/10.1017/s0022112088001429.
Von Kármán, Th., 1911. Ueber den mechanismus des Widerstandes, den ein bewegter Körper in einer flüssigkeit erfährt. Gött. Nachr. 1911, 509–517. PURL: http://resolver.sub.uni-goettingen.de/purl?PPN252457811_1911.
Wang, J., Fan, D., Lin, K., 2020. A review on flow-induced vibration of offshore circular cylinder. J. Hydrodyn. 32, 415–440. https://doi.org/10.1007/s42241-020-0032-2.
Wang, Y.P., Atkins, M.D., Lu, T.J., Kim, T., 2025. Switching events of shed wakes from two short flapping side-by-side cylinders. ASME J. Fluids Eng. 147 (5), 051301. https://doi.org/10.1115/1.4067191.
Wang, Z.J., Zhou, Y., 2005. Vortex interaction in a two side-by-side cylinder near-wake. Int. J. Heat. Fluid Flow. 26 (3), 362–377. https://doi.org/10.1016/j.ijheatfluidflow.2004.10.006.
Wei, T., Smith, C.R., 1986. Secondary vortices in the wake of circular cylinders. J. Fluid Mech. 169, 513–533. https://doi.org/10.1017/s0022112086000733.
Westerweel, J., 1997. Fundamentals of digital particle image velocimetry. Meas. Sci. Technol. 8 (12), 1379–1392. https://doi.org/10.1088/0957-0233/8/12/002.
Westerweel, J., 2000. Theoretical analysis of the measurement precision in particle image velocimetry. Exp. Fluid. 29 (Suppl 1), S003–S012. https://doi.org/10.1007/s003480070002.
Wieselsberger, C., 1922. New data on the law of fluid resistance. NASA Report, taken from Physikalische Zeitschrift, 1921, vol. 22, 321–328. Report number: nACA-TN-84.
Williamson, C.H.K., 1989. Oblique and parallel modes of vortex shedding in the wake of a circular cylinder at low Reynolds numbers. J. Fluid Mech. 206, 579–627. https://doi.org/10.1017/s0022112089002429.
Williamson, C.H.K., 1996. Vortex dynamics in the cylinder wake. Annu. Rev. Fluid Mech. 28, 477–539. https://doi.org/10.1146/annurev.fl.28.010196.002401.
Zdravkovich, M.M., 1969. Smoke observations of the formation of a Kármán vortex street. J. Fluid Mech. 37 (3), 491–496. https://doi.org/10.1017/s0022112069000681.
Zdravkovich, M.M., 1985. Flow induced oscillations of two interfering circular cylinders. J. Sound Vib. 101 (4), 511–521. https://doi.org/10.1016/s0022-460x(85)80068-7.
Zdravkovich, M.M., 1988. Review of flow interference between two circular cylinders in various arrangement. ASME J. Fluids Eng. 9 (4), 618–633. https://doi.org/10.1115/1.3448871.
Zdravkovich, M.M., 1997. Flow Around Circular cylinders, Vol. 1: Fundamentals. Oxford University Press Inc., New York https://doi.org/10.1115/1.2819655.